PHYSICAL REVIEW C **94**, 024912 (2016)

Energy, centrality, and momentum dependence of dielectron production at collider energies in a coarse-grained transport approach

Stephan Endres,* Hendrik van Hees, and Marcus Bleicher
Frankfurt Institute for Advanced Studies, Ruth-Moufang-Straße 1, D-60438 Frankfurt, Germany
and Institut für Theoretische Physik, Universität Frankfurt, Max-von-Laue-Straße 1, D-60438 Frankfurt, Germany
(Received 21 April 2016; published 17 August 2016)

Dilepton production in heavy-ion collisions at collider energies—i.e., for the Relativistic Heavy Ion Collider (RHIC) and the Large Hadron Collider (LHC)—is studied within an approach that uses coarse-grained transport simulations to calculate thermal dilepton emission applying in-medium spectral functions from hadronic many-body theory and partonic production rates based on lattice calculations. The microscopic output from the Ultrarelativistic Quantum Molecular Dynamics (UrQMD) model is hereby put on a grid of space-time cells, which makes it possible to extract the local temperature and chemical potential in each cell via an equation of state. The resulting dilepton spectra are in good agreement with the experimental results for the range of energies available at RHIC, $\sqrt{s_{NN}} = 19.6$–200 GeV. The comparison of the data with the outcome from the coarse-grained UrQMD simulations shows that the newest measurements by the PHENIX and STAR Collaborations are consistent and that the low-mass spectra can be described by a cocktail of hadronic decay contributions together with thermal emission from broadened vector-meson spectral functions and from the quark-gluon plasma phase. Predictions for dilepton results at LHC energies show no significant change of the spectra as compared to RHIC, but a higher fraction of thermal contribution and harder slopes of the transverse-momentum distributions owing to the higher temperatures and flow obtained.

DOI: 10.1103/PhysRevC.94.024912

I. INTRODUCTION

A better understanding of the phase structure of strongly interacting matter given by the fundamental theory of quantum chromodynamics (QCD) is one of the main goals of heavy-ion experiments at ultrarelativistic energies [1–5]. The collision of two nuclei produces a fireball of hot and dense matter, which typically lives for a time span of several fm/c until the system has cooled, owing to collective expansion, to a point where the single particles do not further interact (freeze-out) [6]. The trajectory of the system within the QCD phase diagram is determined by the collision energy: While for lab-frame energies of few GeV one obtains rather low temperatures but finds high values of baryochemical potential, the situation becomes different when going to much higher collision energies; here the temperature increases while the baryochemical potential decreases.

Because hadronic observables usually only reflect the properties of the system at the moment of freeze-out, electromagnetic probes are the appropriate tool to obtain information from the earlier stages of the reaction, when the system is at high temperatures and/or net-baryon densities [7,8]. Photons and dileptons do not interact strongly, therefore they leave the fireball undisturbed once they are produced. However, in consequence the measurement of electromagnetic probes always provides only a time integral over the various stages and sources during the evolution of the reaction. From the theoretical viewpoint the understanding of the production of electromagnetic probes in a heavy-ion collision is complicated by the fact that the evolving fireball of hot and dense matter is not a static but a highly dynamical nonequilibrium system. However, no fully self-consistent approach to describe the in-medium dilepton production for the out-of-equilibrium case is available today. Consequently, one has to apply model descriptions, which always means a reduction of the complexity of the problem to a level where it can be solved.

While hydrodynamic [9,10] and fireball models [11,12] are, in general, successful in describing the measured dilepton spectra by the STAR [13–15] and PHENIX [16] Collaborations at the Relativistic Heavy Ion Collider (RHIC), these models completely rely on a macroscopic description of the fireball. The application of thermal emission rates is usually straightforward in these models, but they require external assumptions such as an initial state and an additional description for the final-state interactions. Besides, their application at lower temperatures and densities is questionable. However, a full microscopic description of the electromagnetic emission—as it is realized in transport models [17–21] based on kinetic theory—is theoretically challenging, especially at very high collision energies. On the one hand, a fully coherent implementation of the different interfering processes and a correct off-shell treatment of the particles has not yet been obtained; on the other hand, it is also still unknown how the microscopic transition from the hadronic to the partonic phase (and vice versa) is actually realized in QCD. Nevertheless, there exist several approaches which aim for such an advanced microscopic description including off-shell and medium effects [22–28].

The coarse-graining approach, which is used in the present work for the theoretical calculation of dilepton production, is based on the concepts presented in Ref. [29] and has been successfully applied to describe spectra of electromagnetic probes at energies available at the GSI Schwerionensynchrotron

*endres@th.physik.uni-frankfurt.de

(SIS 18), the Facility for Antiproton and Ion Research (FAIR), and the CERN Super Proton Synchrotron (SPS) [30–33]. It offers a compromise between the microscopic and macroscopic description of the collision evolution. On the one hand, the dynamics is here based on a purely microscopic description from the Ultrarelativistic Quantum Molecular Dynamics (UrQMD) model [34,35]; on the other hand, the "coarse-graining" (i.e., the reduction of the large amount of information regarding the phase-space coordinates of the single hadrons)—performed by averaging over a large ensemble of events and extracting the local thermodynamic properties of the system—makes it possible to describe the reaction dynamics in macroscopic terms of temperature and chemical potential. The approach has the advantage that it is, in principle, applicable to all phases of a heavy-ion collision and also works for lower collision energies where the use of other macroscopic models is questionable.

For the present paper previous studies are extended to energies available at RHIC and the Large Hadron Collider (LHC), which cover the range of center-of-momentum energies from $\sqrt{s_{NN}} = 19.6$ GeV up to 5500 GeV. In this energy regime the net-baryon density is assumed to be close to zero for the greatest part of the fireball evolution, and a significant amount of the electromagnetic emission will stem from the quark-gluon plasma (QGP). The specific conditions found at these collision energies offer the possibility to study—among others—the following issues.

(i) The experimental dilepton measurements will show whether the hadronic spectral functions, which have proven to successfully describe the low-mass dilepton excess, are also consistent with the conditions found in heavy-ion collisions at collider energies, where the baryochemical potential is significantly lower than the temperature for the greatest part of the reaction evolution. Previous work has shown that the in-medium effects on the spectral properties of baryon resonances should still play an important role because the modification of vector mesons is governed by the *sum* of the baryon and antibaryon densities, not the net density [11].

(ii) At higher invariant masses ($M_{e^+e^-} > 1$ GeV/c^2) correlated open-charm decays give a significant contribution to the measured dilepton yield for RHIC and LHC energies [36]. Similar to the light vector mesons, whose spectral shape is modified in the medium, the charm contribution is known to be affected by the presence of a hot and dense medium [37–39]. However, it is unclear how strong these effects are. A direct measurement is difficult, as one also finds a strong thermal contribution from the QGP in that mass region. It is therefore an important theoretical task to disentangle the different contributions and to provide a comprehensive description of the measured dilepton spectra. Although we do not consider charm contributions in the present study, the thermal results for the QGP contribution may serve as a baseline and help to limit the possible medium modifications for D and $\bar{D}$ mesons.

(iii) Owing to the very high temperatures reached at the collider energies considered here, the partonic contribution to the overall dilepton yield will be very significant. This might facilitate to study the properties of the quark-gluon plasma, e.g., its temperature [11,40].

(iv) Further, it will be interesting whether the reaction dynamics of the colliding system shows deviations as compared to the situation at lower energies. Large parts of the evolution are dominated by temperatures above the critical temperature, in contrast to the situation at SPS and, even more, SIS 18 or FAIR. Experimental results for RHIC exhibited an unexpected large flow for direct photons, which is not fully explained by theory up to now [41,42]. With regard to the coarse-graining approach, it will be especially interesting to see in how far the underlying microscopic dynamics, which is completely hadronic, can account for the correct expansion of the system and the time-evolution of temperature and chemical potential.

The last aspect also points out a caveat. Whereas the creation of a deconfined phase with free quarks and gluons is assumed to take place in the early stages of heavy-ion collisions at RHIC and LHC energies, the microscopic dynamics from UrQMD does not include a description of this partonic phase. Nevertheless, we argue that it is possible to extract a reasonable and realistic picture of the fireball evolution and thermal electromagnetic emission also at RHIC and LHC energies, including a description of emission from a QGP phase. While a lattice equation of state (EoS) and partonic rates can be applied to approximate the thermodynamic properties and emission patterns inside a partonic phase, it is, however, clear that the fireball evolution itself from the coarse-grained dynamics cannot reflect any effects owing to the creation of a quark-gluon plasma on the microscopic level. Although it is assumed that the influences of a phase-transition or crossover on the gross microscopic evolution are not very significant, this is, of course, a limiting factor of the present model. Nevertheless, the results might help to understand if and how the phase structure of QCD is reflected in the microscopic dynamics, if the comparison of the model outcome to experimental data shows significant deviations.

This paper is structured as follows. In Sec. II the coarse-graining approach is introduced, and the various dilepton-production mechanisms, which enter the calculations, are outlined. This is followed by a presentation of the results for the space-time evolution of the reaction (Sec. III A) and dilepton spectra for energies available at RHIC and LHC (in Secs. III B and III C). A comparison of the results for RHIC and LHC is given in Sec. III D. Finally, we conclude with a summary and an outlook to further studies in Sec. IV.

II. THE COARSE-GRAINING APPROACH

In the following, the basic features of the coarse-graining approach are outlined. This description is kept concise here, as the same model was presented in detail previously; for details, we refer the reader to Refs. [30,31].

A. Microscopic simulations

As a first step, simulations for the different collision energies are conducted with the present version 3.4 of the UrQMD approach [34,35,43,44], a semiclassical hadronic transport model based on the principles of kinetic theory, in which the evolution of a heavy-ion collision is described by the propagation of on-shell particles on classical trajectories in combination with a probabilistic treatment of the individual hadron-hadron scatterings. It constitutes an effective solution of the Boltzmann equation, where the collision term includes elastic and inelastic scatterings, as well as resonance decays. To account for quantum effects, the particles are represented by Gaussian wave packets and effects such as Pauli blocking are included. For hadron-hadron collisions with energies above $\sqrt{s} = 3$ GeV the excitation of strings is possible. The model includes all relevant meson and baryon resonances up to a mass of 2.2 GeV/c^2. Resonance parameters and cross sections are adapted and extrapolated to the values collected by the Particle Data Group [45].

For being able to deduce a realistic fireball evolution in terms of T and μ_B and—in consequence—meaningful dilepton spectra from the UrQMD simulation, one first has to check whether the model can describe the bulk results measured in experiment. In general, the UrQMD model has proven to reproduce the hadronic observables from heavy-ion reactions very well in a wide range of collision energies. Also up to RHIC and LHC energies the hadron production and the resulting yields, ratios, rapidity, and transverse-momentum spectra are quite well described in the approach; for details, we refer the reader to Refs. [43,46,47]. However, looking at specific observables one also finds deviations of the model results from the experimental data. This is especially the case for the elliptic flow, v_2: Whereas the elliptic flow is described quite well up to SPS energies, for higher collision energies the average elliptic flow $\langle v_2 \rangle$ underestimates the experimental results. At top RHIC energy of $\sqrt{s_{NN}} = 200$ GeV the transport model reaches only roughly 60% of the measured value [48]. Regarding the transverse-momentum dependence of v_2, the underprediction is most prominent for high p_t [49–51]. Nevertheless, the model reproduces the centrality dependence and the gross features of the v_2 particle-type dependence, such as the mass ordering for low p_t and the number-of-constituent-quark scaling for higher transverse momenta [52]. Because the buildup of v_2 in the model correlates to the rescattering rate, the low values of this observable in UrQMD as compared to the data can be interpreted as a hint that a strongly interacting phase of partons is created in the early reaction evolution [53–55] (see also Sec. II C).

However, the anisotropic flow effects are very small (at the order of few percent) and have only very little influence on the dilepton invariant-mass and transverse-momentum spectra. In consequence, the deviations from the experimental measurements will not play a significant role for our present study. This is, of course, different for studies of the anisotropic flow of electromagnetic probes, where the deviations from the measured bulk v_2 will be apparent. To reproduce these measurements, one will probably need an advanced description which includes the effects of the partonic phase on the fireball evolution.

B. Extracting thermodynamic properties

Within the UrQMD model one has a well-determined phase-space distribution function $f(\vec{x},\vec{p},t)$, as the location and momenta of all particles are known. However, because the full microscopic treatment of the medium effects is quite complicated, the present approach aims to reduce (i.e., to coarse grain) the amount of information given by $f(\vec{x},\vec{p},t)$, such that one can switch from a microscopic to a macroscopic description of the collision. Instead of the individual particle coordinates, the system is then defined by its thermodynamic properties. To do so, it is first necessary to obtain a smooth distribution function, which is realized by averaging over a large number of events:

$$f(\vec{x},\vec{p},t) = \left\langle \sum_h \delta^{(3)}[\vec{x} - \vec{x}_h(t)]\delta^{(3)}[\vec{p} - \vec{p}_h(t)] \right\rangle. \quad (1)$$

Here the angle brackets $\langle\cdot\rangle$ denote the ensemble average. It is important to bear in mind that the UrQMD model constitutes a nonequilibrium approach, whereas the thermodynamic properties are well defined only for equilibrated matter. Consequently, the approximate extraction of equilibrium quantities is consistent only locally. Thus, a grid of small space-time cells is set up where—following Eq. (1)—for each of these cells the energy-momentum tensor and the baryon current are extracted as

$$T^{\mu\nu} = \frac{1}{\Delta V}\left\langle \sum_{i=1}^{N_h \in \Delta V} \frac{p_i^\mu \cdot p_i^\nu}{p_i^0} \right\rangle,$$
$$j_B^\mu = \frac{1}{\Delta V}\left\langle \sum_{i=1}^{N_{B/\bar{B}} \in \Delta V} \pm\frac{p_i^\mu}{p_i^0} \right\rangle. \quad (2)$$

Here ΔV is the volume of the cell and the sum is taken over all (anti-)baryons or hadrons in the cell, respectively. If one knows j_B^μ and $T^{\mu\nu}$, the local rest frame (LRF) can be determined by applying the definition of Eckart [56], which requires a vanishing baryon flow, $\vec{j}_B = 0$. The energy density of the cell is then defined as $\varepsilon = T^{00}_{\mathrm{LRF}}$ and the net-baryon density is $\rho_B = j^0_{B,\mathrm{LRF}}$.

To obtain temperature and baryochemical potential, it is necessary to apply an EoS which translates the local energy and baryon densities into T and μ_B, respectively. For consistency with the underlying transport model, we apply a hadron gas EoS [57] for the lower temperature range up to $T = 170$ MeV. It includes the same hadronic degrees of freedom as the UrQMD approach. For higher temperatures, a pure hadronic description is insufficient, as the phase transition to a quark-gluon plasma also changes the degrees of freedom and consequently the equation of state. We therefore use an EoS from lattice calculations [58] (with a critical temperature $T_c = 170$ MeV) for cells with higher energy densities. While both EoSs match in the temperature region from 150 to 170 MeV, the lattice EoS gives significantly higher temperatures for very hot cells. A comparison between both equations of state is given in Ref. [30].

It is important to bear in mind that the application of the lattice EoS for higher energy densities or temperatures, respectively, does not provide full consistency with the

underlying hadronic dynamics in the transport model; in UrQMD only hadronic degrees of freedom are implemented, and no phase transition to a partonic phase is included. However, the very details of the microscopic dynamics are anyway "washed out" in the coarse-graining procedure by the reduction of the multitude of information and the averaging over the events. Because we only use the local energy density distribution from the microscopic simulations to calculate a temperature via the lattice EoS ($\mu_B = \mu_\pi = 0$ is always assumed for $T > 170$ MeV), a severe problem should arise only if the gross evolution of the density distribution would largely depend on the specific equation of state. This would imply differences in the measurable particle spectra. However, previous studies with a UrQMD + hydrodynamics hybrid model [59] have shown that the bulk evolution of the fireball is not significantly altered when using an EoS including a phase transition instead of a pure hadron gas EoS [60]. Taking this into account, the procedure as applied in the present approach seems justifiable. (The effect of the choice of EoS on the dilepton spectra is also studied in Sec. III B.)

C. Nonequilibrium effects

The approach as outlined above assumes a locally equilibrated system in each cell. However, it is clear that within a transport approach this condition is not always fulfilled in a satisfying manner. In contrast, owing to the nonequilibrium nature of the model, one finds significant deviations from kinetic and/or chemical equilibrium. For a correct description of the fireball evolution the consequences of these deviations need to be considered. Basically, one finds two dominant effects which affect the thermodynamic properties and, consequently, the dilepton emission.

(1) Pressure isotropy is necessary for a system to be in *kinetic equilibrium*. However, it is well known from previous studies [61,62] that the initial stages of a heavy-ion collision are dominated by large differences between the longitudinal and transverse pressures. This is a consequence of the strong longitudinal compression of the nuclei at the beginning of the collision. In this case, the energy density is overestimated in the cell because a large fraction of the energy is of no relevance with regard to the thermal properties of the system. To apply the coarse-graining approach also for the first few fm/c of the collision, it is therefore necessary to extract a realistic energy density ε_{eff} taking the limited degree of thermalization into account. This is achieved by the use of a generalized equation of state for a Boltzmann-like system [63,64], which gives ε_{eff} in dependence on the "bare" energy density in the cell and the pressure anisotropy. The results for SPS energies showed that significant deviations of ε_{eff} are only found for the first 1–2 fm/c of the collision [30].

(2) *Chemical nonequilibrium* shows up in the form of finite meson chemical potentials (in full equilibrium, all meson chemical potentials vanish as the meson number is not a conserved quantity, in contrast to, e.g., the net-baryon number) and most dominantly in the form of a pion chemical potential μ_π, because the π mesons are the most abundantly produced particles. A finite μ_π is the consequence of an overpopulation of pion states. In a transport model, such an overdense pion system is especially found at the very beginning of the reaction, when the fireball is still far from kinetic equilibrium and the first inelastic collisions produce a large number of pions [65]. The pion chemical potential is important for the population of ρ and ω vector mesons, as a high density of pions increases the probability for the production of these particles (besides, μ_π has also some moderate effects on the spectral shape) [66,67]. To account for these effects, we extract the pion chemical potential in each cell in Boltzmann approximation.

When the local energy and particle densities change in the course of the fireball evolution, the phase-space distribution function, $f(\vec{x},\vec{p},t)$, is adjusted to the corresponding values of temperature and chemical potentials. If this adjustment is slower than the change of T and μ, one will find deviations from the local equilibrium distribution of the form [68]

$$f(\vec{x},\vec{p},t) = f_{\text{eq}}(\vec{x},\vec{p},t) + \delta f(\vec{x},\vec{p},t). \tag{3}$$

One consequence of this deviation from the equilibrium state is the appearance of finite transport coefficients, such as viscous stresses, heat flow, and diffusion [69]. Note that in the underlying transport dynamics used for the coarse graining these effects are implicitly implemented owing to the nonzero mean free path of the interacting hadrons. The resulting transport coefficients (e.g., viscosity and heat conductivity) from UrQMD have been in detail studied for the infinite-matter case in box calculations [70–73]. The results showed that for the shear-viscosity-to-entropy ratio one obtains rather high values $\eta/s > 0.6$ within the model. This is in contrast to ideal hydrodynamic calculations which have been quite successful in describing the observables from heavy-ion collisions by neglecting the effect of those transport coefficients. The large elliptic flow measured in noncentral heavy-ion reactions at RHIC energies suggests a very low value of the shear viscosity to entropy ratio η/s in the created hot and dense fireball. This was interpreted as a direct hint for the creation of a quark-gluon plasma phase early during the fireball evolution [74,75]. The high values of η/s from UrQMD can, in consequence, explain the underestimation of the resulting elliptic flow v_2 at RHIC in the model, as discussed in Sec. II A.

However, recently the role and importance of viscosity has come into theoretical focus and was studied intensively in hydrodynamical approaches [76–81], as it was found that pure ideal hydrodynamic calculations result in an overestimate of the elliptic flow for high transverse momenta and/or wrong slopes for the hadron-p_t spectra [68]. With regard to the dilepton emission, the appearance of a shear viscosity might show an effect in two ways: First, by its influence on the bulk evolution (especially an increase of the directed flow and a reduction of the anisotropies) and, second, by the direct modification of the emission rates owing to modifications of the distribution functions [82].

Whereas the coarse-grained dynamics of the fireball naturally reflects the viscosities in the underlying microscopic

simulations, as mentioned above, we do not consider the effects of the viscous corrections on the electromagnetic emission rates for two reasons: On the one hand, it was shown that the influence of finite viscosity on the resulting invariant mass or transverse-momentum spectra of dileptons and photons is rather small, especially for the low-mass region up to 2 GeV/c^2 [9,10,83]. (The case is somewhat different for the elliptic flow, where the modification of the emission rates might be more pronounced.) On the other hand, there are presently no calculations available for the hadronic and partonic rates which are applied in our approach. The viscous correction for emission from the quark-gluon plasma has so far only been calculated for the perturbative Born rate, i.e., for leading-order $q\bar{q}$ annihilation [84]. However, this rate is known to significantly underestimate the thermal yield for lower masses, compared to more advanced hard-thermal loop or lattice rates [85,86]. The situation is similar for the hadronic rates, where the effect of viscosity has been considered only for a low-density calculation [87] which cannot account for the full in-medium modifications of the vector mesons' spectral shape.

We discuss the emission rates applied in the present approach in detail in the following Sec. II D.

D. Thermal dilepton rates

The thermal emission of dileptons from an equilibrated system of hot and dense matter is determined by the imaginary part of the (retarded) electromagnetic current-current correlation function, $\mathrm{Im}\Pi_{\mathrm{em}}^{(\mathrm{ret})}$, which is connected to the electromagnetic current j_μ [88]. The dilepton yield per four-volume and four-momentum can then be calculated according to the relation [67,89]

$$\frac{dN_{ll}}{d^4x d^4q} = -\frac{\alpha_{\mathrm{em}}^2 L(M)}{\pi^3 M^2} f_{\mathrm{B}}(q;T)\mathrm{Im}\Pi_{\mathrm{em}}^{(\mathrm{ret})}(M,\vec{q};\mu_B,T), \quad (4)$$

where f_{B} is the Bose distribution function and $L(M)$ the lepton phase space.

In the hadronic low-mass regime (i.e., for $M_{e^+e^-} < 1$ GeV/c^2) the electromagnetic current directly couples to the vector mesons and—assuming vector-meson dominance (VMD)—Π_{em} is proportional to the vector-meson propagator

$$D_V = \frac{1}{q^2 - m_V^2 - \Sigma_V(q^2)}, \quad (5)$$

where m_V is the bare mass of the meson and Σ_V the corresponding self-energy of the particle, related to its decay width. Whereas the self-energy in the vacuum can be deduced from experimental measurements of inelastic electron-positron scattering ($e^+e^- \to$ hadrons), the situation for finite T and μ_{B} is more complicated and requires detailed model calculations. For the present work we apply the results from equilibrium quantum-field theory calculations with a hadronic many-body approach [90,91]. They account for the interactions of the ρ and ω mesons with hadrons in a heat bath. For the ρ the pion cloud ($\Sigma_{\rho\pi\pi}$) as well as the direct contributions from ρ-hadron scatterings with baryons ($\Sigma_{\rho B}$) and mesons ($\Sigma_{\rho M}$) are included in the calculation of the in-medium self-energy. In this case Eq. (5) becomes

$$D_\rho = \frac{1}{M^2 - m_\rho^2 - \Sigma_{\rho\pi\pi} - \Sigma_{\rho B} - \Sigma_{\rho M}}. \quad (6)$$

The situation for the ω meson is more complex, as it constitutes a three-pion resonance. Here the self-energy includes $\omega \to \pi\rho$ and $\omega \to 3\pi$ decays as well as the inelastic $\omega\pi \to \pi\pi, \omega\pi \to b_1$, and $\omega N \to N^*$ scatterings. The resulting propagator reads

$$D_\omega = \big[M^2 - m_\omega^2 + \mathrm{i}m_\omega(\Gamma_{3\pi} + \Gamma_{\rho\pi} + \Gamma_{\omega\pi\to\pi\pi}) - \Sigma_{\omega\pi b_1} - \Sigma_{\omega B}\big]^{-1}. \quad (7)$$

To account for the symmetry of the interactions of ρ and ω mesons with baryons and antibaryons, the spectral functions do not depend on the baryochemical potential μ_B but on an effective baryon density $\rho_{\mathrm{B}}^{\mathrm{eff}} = \rho_{\mathrm{N}} + \rho_{\bar{\mathrm{N}}} + 0.5(\rho_{\mathrm{B}^*} + \rho_{\bar{\mathrm{B}}^*})$ [92]. Here $\rho_{\mathrm{N}/\bar{\mathrm{N}}}$ denotes the nucleon/antinucleon density and $\rho_{\mathrm{B}^*/\bar{\mathrm{B}}^*}$ is the density of excited baryon/antibaryon resonances.

Note that in the case of a finite pion chemical potential an additional fugacity factor,

$$z_\pi^n = \exp\left(\frac{n\mu_\pi}{T}\right), \quad (8)$$

enters in Eq. (4). The exponent n depends on the difference between initial and final pion numbers for the relevant channel [67,93,94]. For dilepton production from ρ mesons one has $n = 2$, whereas for the ω it is $n = 3$.

At the higher masses above 1 GeV/c^2 one no longer finds distinct resonances in the hadronic domain of the vector channel but a broad continuum of multipion states which couple to the electromagnetic current. In principle, also here the dilepton emission is related to the vector spectral function. However, the presence of pions at finite T causes a chiral mixing of the isovector part of the vector and axial-vector correlators [95]. The corresponding isovector-vector current correlation function takes the form [96]

$$\Pi_V(p) = (1-\varepsilon)z_\pi^4 \Pi_{\mathrm{V},4\pi}^{\mathrm{vac}} + \frac{\varepsilon}{2} z_\pi^3 \Pi_{\mathrm{A},3\pi}^{\mathrm{vac}} + \frac{\varepsilon}{2}\left(z_\pi^4 + z_\pi^5\right)\Pi_{\mathrm{A},5\pi}^{\mathrm{vac}}, \quad (9)$$

where the mixing coefficient ε is given by the thermal pion loop, and z_π again denotes the pion fugacity.

For temperatures above the critical temperature T_c the relevant degrees of freedom are no longer hadrons (vector mesons) but quarks and gluons. In this situation the strength of the electromagnetic current is accounted for by a partonic description and the thermal dilepton production occurs—to leading order—via the electromagnetic annihilation of quark-antiquark pairs, $q\bar{q} \to \gamma^*$. However, it has been shown that the pure pQCD result [84] underestimates the actual dilepton emission in the low-energy regime (i.e., at low masses). Nonperturbative results indicate a strong enhancement owing to α_s corrections and bremsstrahlung effects [85]. In the present work we apply a spectral function from lattice QCD calculations [86] which has been extrapolated for finite three-momenta by a fit to the according photon rate [11]. Note that these lattice rates are available only for vanishing quark chemical potential $\mu_q = 0$. However, the effects of a finite μ_q

are quite small with regard to the dilepton emission rates and can be neglected here.

E. Nonthermal hadronic decay contributions

In addition to the thermal dilepton emission from the hot and dense fireball, there are also contributions from more long-lived mesons which mostly decay into lepton pairs after the freeze-out of the system, mainly the pseudoscalar π^0 and η mesons. Their Dalitz decays into a real and a virtual photon (which subsequently transforms in a lepton pair) dominate the very low invariant masses. The corresponding decay width is related to the probability for the decay into two photons and given by the Kroll-Wada formula [97],

$$\frac{d\Gamma_{P\to\gamma e^+e^-}}{dM} = \frac{2\alpha}{3\pi M}\, L(M)\, 2\Gamma_{P\to\gamma\gamma}\left(1-\frac{M^2}{M_\rho^2}\right)|F_{P\gamma\gamma^*}(M^2)|, \tag{10}$$

where the form factors $F_{P\gamma\gamma^*}$ are fitted to experimental data [98], consistent with the theoretical results assuming VMD.

Note that only the final state π and η mesons are considered for the procedure. Those mesons which are produced and absorbed again during the collision have a negligible probability for a dilepton decay owing to their small decay width. The situation is somewhat different for the ϕ meson. In spite of the shorter lifetime, we do not treat it as a thermal contribution (because the expected medium effects are so small that they can be neglected) but consider the microscopic decays here as for the pseudoscalar mesons. However, in this case one assumes that the ϕ has an equal probability for the decay into a lepton pair at any time and therefore can continuously emit dileptons [99]. The total yield is then obtained as a time integral over the lifetime as

$$\frac{dN_{ll}}{dM} = \frac{\Delta N_{ll}}{\Delta M} = \sum_{i=1}^{N_{\Delta M}}\sum_{j=1}^{N_\phi}\int_{t_i}^{t_f}\frac{dt}{\gamma}\frac{\Gamma_{\phi\to ll}(M)}{\Delta M}, \tag{11}$$

where the γ factor accounts for the relativistic time dilation in the computational frame compared to the mesons rest frame. This procedure explicitly takes absorption processes for the ϕ into account.

Besides, two more nonthermal contributions arise owing to the fact that not for all cells is it possible to properly calculate the thermal contribution. This is mainly the case for the later stages of the reaction, for cells with (i) no baryon content, so that the LRF is not well defined, or (ii) where the temperature is below 50 MeV, in which case the EoS and the emission rates no longer give reliable results. In these cases a "freeze-out" contribution for the ρ and ω meson is determined directly from the microscopic UrQMD results for those specific cells. The procedure is the same as for the ϕ given by Eq. (11), but the time integration is performed only for the corresponding time-step size.

III. RESULTS

For the present study the coarse graining of the UrQMD transport output was performed with ensembles of 1000 UrQMD events for Au + Au collisions at RHIC and 500 events for Pb + Pb reactions at LHC energies. The time-step size was chosen as $\Delta t = 0.4$–0.6 fm/c, and the spatial dimensions of the cell are defined as $\Delta x = \Delta y = \Delta z = 0.8$–$0.9$ fm, depending on the collision energy. The impact parameter distributions corresponding to different centrality classes were chosen using Glauber-model fits to experimental data [14,16]. Note that the minimum bias definitions differ slightly between the STAR and PHENIX collaborations; the former uses 0%–80% most central collisions, whereas the PHENIX trigger takes 0%–92% central collisions into account.

A. Fireball evolution

The thermal dilepton emission from a hot and dense fireball created in a heavy-ion collision is determined by the trajectory of the system within the QCD phase diagram. More precisely, because for each space-time cell different values of temperature and baryochemical potential are obtained within the coarse-graining approach, the overall yield is directly related to the distribution of the thermal four-volume V_4 inside the fireball with regard to T and μ_B. Figure 1(a) shows the total thermal four-volume summed over all cells in dependence on the respective temperature for Au + Au and Pb + Pb reactions at four different collision energies, from the lowest RHIC to top LHC energies. While for the low-temperature range around 100 MeV the differences between the energies are not larger than one order of magnitude, the relative increase of the number of higher temperature cells is much stronger. For $\sqrt{s_{NN}} = 19.6$ GeV one hardly finds cells with temperature above 300 MeV, while at LHC energies there are some cells with up to 800 MeV (few rare cells even reach still higher temperatures up to 1000 MeV, which is not shown here).

When considering the μ_B dependence of the four-volume for the temperature range from 120 to 170 MeV in Fig. 1(b), one also finds that the average baryon chemical potential is decreasing when going to higher collision energies (note again, as outlined in Sec. II B, that the lattice EoS for $T > 170$ MeV, in general, assumes vanishing baryochemical potential). At $\sqrt{s_{NN}} = 19.6$ GeV the most abundant μ_B range lies between 200 and 300 MeV, whereas at LHC μ_B is close to zero for the overwhelming part of the thermal four-volume. It is interesting that one gets a slightly stronger contribution from higher chemical potential when going from 2.76 to 5.5 GeV. However, this might be an effect owing to the limited temperature window considered here.

The resulting time evolution of the thermal dilepton emission dN/dt from all cells (and from those with temperature above 250 MeV only) is shown in Fig. 2. The results for central (0%–10%) Au + Au reactions at 200 GeV and Pb + Pb collisions at 2.76 TeV exemplarily expose the similarities and differences in the fireball dynamics for RHIC and LHC. In general, one observes that the evolution of the fireball for both energies is very similar, apart from the larger overall emission at 2.76 TeV compared to the 200-GeV case. This is a consequence of the larger thermal four-volume for all temperature regions; compare Fig. 1(a). However, at the LHC the cooling of the system is slower, especially the emission from the very hot cells with $T > 250$ MeV shows a less significant drop

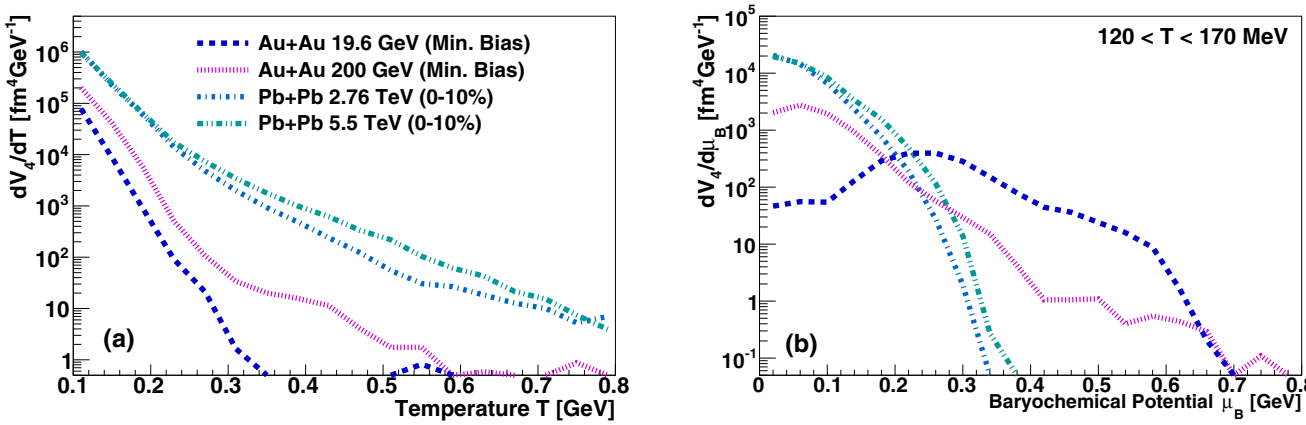

FIG. 1. Thermal four-volume V_4 in dependence on temperature (a) and baryochemical potential (b) for Au + Au and Pb + Pb reactions at different collision energies.

than for the RHIC energy. In any case, the thermal emission from the later stages of the reaction—even 40–50 fm/c after the first initial nucleon-nucleon interactions—is remarkably large, although the influence on the total yield is very small, as dN/dt is suppressed by one to two orders of magnitude compared to the early maxima.

B. Relativistic Heavy Ion Collider

The dilepton invariant-mass spectra for minimum-bias Au + Au reactions at the two RHIC energies $\sqrt{s_{NN}} =$ 19.6 and 200 GeV are presented in Fig. 3. The results as obtained with the coarse-graining approach are compared to the experimental data from the STAR Collaboration [14]. The spectra are shown within the STAR acceptance, which means rapidity and pseudorapidity cuts ($|\eta^e| < 1$, $|y^{ee}| < 1$) were applied for single electrons and dileptons, respectively,

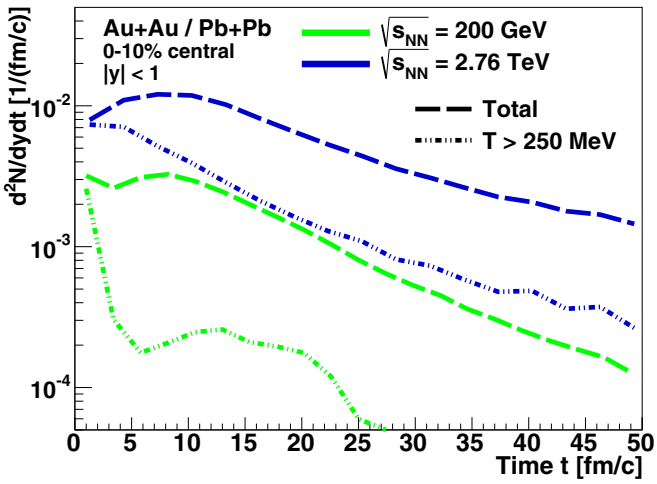

FIG. 2. Time evolution of the thermal dilepton emission $dN_{e^+e^-}/dt$ for central Au + Au collisions at $\sqrt{s_{NN}} = 200$ GeV (green lines) and Pb + Pb collisions at $\sqrt{s_{NN}} = 2.76$ TeV (blue lines). The total emission (long dashed lines) is shown as well as the resulting yield only from cells with a temperature above 250 MeV (dashed double dotted lines).

together with an additional transverse momentum cut for electrons (i.e., here $p_t^e > 0.2$ GeV). The comparison shows that in both cases the invariant-mass spectra for low masses below 1 GeV/c^2 are very well described within the model. While in relation to pure hadronic decay cocktails an excess of the experimentally measured spectra was observed for the mass region $0.3 < M_{e^+e^-} < 0.7$ GeV/c^2, our approach shows that this region is dominated by thermal emission from the ρ meson and from partonic emission. However, there are also important differences visible when comparing the outcome for both energies: Owing to the larger temperatures obtained for Au + Au reactions at 200 GeV, the low-mass region is here dominated by QGP emission; only around the ρ pole mass is the hadronic emission dominant. In contrast, the thermal ρ contribution clearly outshines the partonic yield for the greatest part of the low-mass region up to 1 GeV/c^2 at the lower collision energy of 19.6 GeV.

It is interesting that the spectral shape of the thermal ρ resembles its vacuum shape in both cases, compared to the very strong broadening and low-mass enhancement which is observed for SIS 18 and FAIR energies [31,32]. However, this is not surprising because in the previous section it has already become clear that the baryochemical potential is rather low in most of the cells. Even if one considers that the baryonic modifications of the spectral shape for the ρ are governed by the effective baryon and antibaryon density, the effects seem relatively small. One reason for this is that the initial heating is faster and stronger at RHIC energies and the early phase of the reaction is mostly dominated by partonic emission (which is quite insensitive with regard to finite quark chemical potential $\mu_q = 1/3\mu_B$), whereas the hadronic contributions are predominantly radiated at later stages when the baryon densities are lower. Consequently, the baryon-induced medium effects—which are the main cause of the ρ low-mass enhancement—are only very moderate here. Note that there is also a significant nonthermal ρ contribution from low-temperature and late-stage cells, which is more dominant for 200 GeV. This might be caused by the longer lifetime of the system, with a significant number of those mesons in peripheral cells and late in the evolution. In contrast to the thermal ρ, the thermal ω contribution is rather negligible

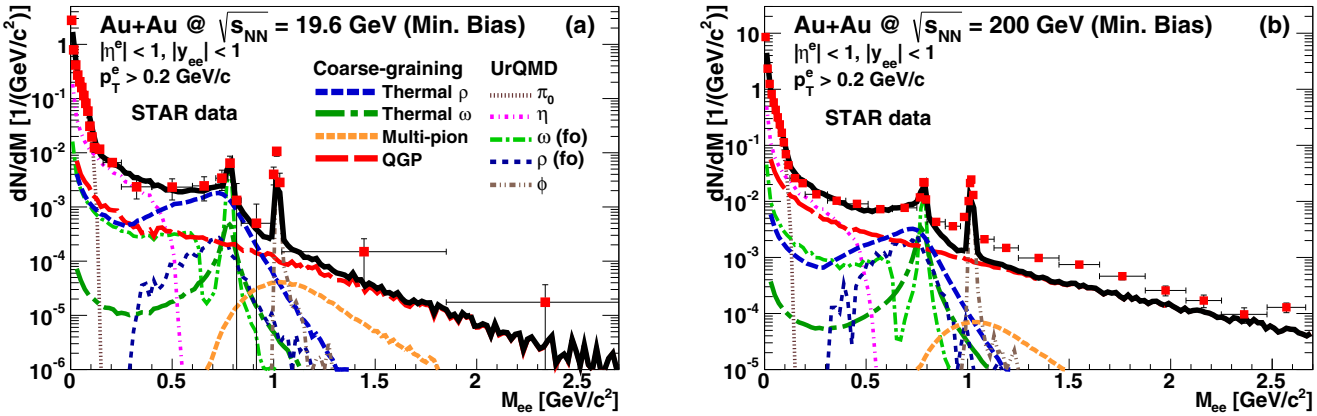

FIG. 3. Dielectron invariant-mass spectra for minimum bias (i.e., 0%–80% most central) Au + Au collisions at $\sqrt{s_{NN}} = 19.6$ GeV (a) and 200 GeV (b). The sum includes the thermal hadronic and partonic emission obtained with the coarse-graining and also the hadronic π, η, and ϕ decay contributions from UrQMD as well as the "freeze-out" contributions (from cold cells) of the ρ and ω mesons. The model results are compared to the experimental data obtained by the STAR Collaboration [14].

compared to the respective freeze-out contribution. This is mainly attributable to the long lifetime of the ω, which is typically so long that this resonance mostly decays outside the hot and dense region.

In contrast to the low-mass region, for $M_{e^+e^-} > 1$ GeV/c^2 the overall dilepton yield is no longer dominated by the peaks from various hadronic decays but one experimentally finds a structureless continuum. In our model the thermal emission from multipion interactions and from the partonic phase shine in this part of the spectrum. Note however that—as mentioned before—the present calculation does not include the Drell-Yan and, more important, the open-charm contributions to the spectrum. Nevertheless, as the strength of possible medium modification for D or $\bar{D}$ mesons is yet unclear, our calculation can serve as a thermal baseline.

For $\sqrt{s_{NN}} = 19.6$ GeV the QGP emission is the dominant contribution in the mass region from 1 to 2.8 GeV/c^2, with a significant contribution from the multipion part, which is strongest around $M_{e^+e^-} = 1.1$ GeV/c^2. Here 20%–30% of the thermal contribution are from the hadronic source, while for higher masses the multipion yield becomes rather insignificant. The comparison with experimental data allows for no clear conclusions at this energy owing to the limited statistics and rather large errors. The yield from the coarse-graining model is within the statistical error of the data but rather at the lower boundary. The situation is somewhat different for Au + Au collisions at 200 GeV. At this higher energy the QGP emission is now the dominant thermal contribution, whereas the hadronic contribution is suppressed by at least a factor of 10 for $M_{e^+e^-} > 1$ GeV/c^2. Owing to the significantly better statistics, one can observe that the model does not fully describe the STAR data, but the dilepton emission obtained within the model makes up for only roughly 50% of the measured yield in the region from 1 to 2 GeV/c^2. Interestingly, for even higher masses the agreement between model and data becomes better; the slope of the thermal emission seems to be slightly harder than the measured one. These results agree with previous studies, indicating that the relative suppression of the charm contribution owing to medium effects is more pronounced at higher masses, leaving it the dominant contribution only for lower masses around 1 GeV/c^2 [39].

While by default we use a combination of a hadron gas and a lattice EoS (HG + LAT-EoS) for all calculations presented in this work, it was discussed in Sec. II B that this is not fully consistent with the underlying purely hadronic microscopic dynamics. In consequence, it is instructive to compare this standard scenario with the more consistent case where only the hadron gas equation of state (HG-EoS) is used for all temperature ranges to extract T and μ_B. Note that in both cases we use the hadronic rates up to $T = 170$ MeV and the partonic emission rates for higher temperatures for being able to directly compare the effect of the different EoS. The total invariant-mass spectra obtained with both EoS are put on top of each other for minimum-bias Au + Au collisions at 200 GeV in Fig. 4. The results indicate that the differences with regard to the overall yield in the low-mass region are rather small and result in no significant deviations in the thermal emission pattern for masses up to $M_{e^+e^-} = 1$ GeV/c^2. The slightly reduced QGP yield in this region owing to the lower temperatures from the HG-EoS is mostly compensated by a larger hadronic contribution, especially around the ρ pole mass. However, the picture is quite different for masses above 1 GeV/c^2, dominated by the QGP emission: Here the use of the HG-EoS results in a significantly lower thermal yield and a softer slope. The yield is suppressed by almost an order of magnitude at $M_{e^+e^-} = 2.5$ GeV/c^2 compared to the HG + LAT-EoS scenario. This is not surprising, because these higher masses are dominated by emission from the very early hot stage of the fireball where the highest energy densities are reached. Here the differences between the two EoSs are most dominant and the lattice equation of state results in significantly higher temperatures. On the one hand, this result indicates that the low-mass dilepton spectra are quite insensitive with regard to the EoS; on the other hand, it shows again that direct information regarding the phase structure of QCD might be deduced from the spectra at higher invariant masses, 1 GeV/$c^2 \lesssim M_{e^+e^-} \lesssim 2.5$ GeV/c^2. However, the experimental extraction of the thermal yield

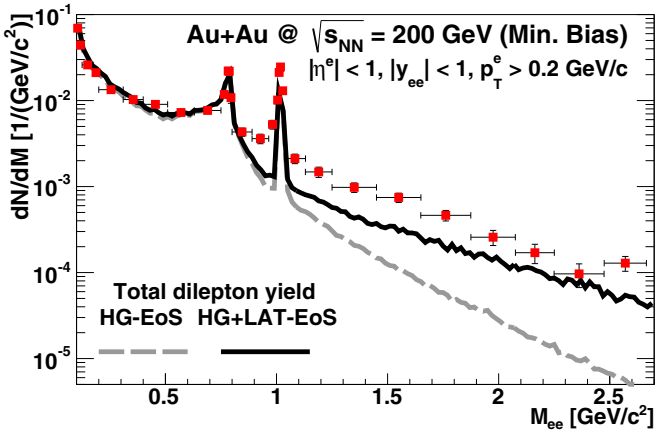

FIG. 4. Comparison of the influence of different EoS on the dielectron invariant-mass spectrum for minimum-bias Au + Au collisions at $\sqrt{s_{NN}} = 200$ GeV. We show the result obtained with a pure hadron gas equation of state (HG-EoS) and the combination of the hadron gas together with a lattice EoS at higher temperatures (HG + LAT-EoS). In both cases the hadronic rates are used up to $T = 170$ MeV and partonic rates for higher temperatures. The model results are compared to the experimental data obtained by the STAR Collaboration [14].

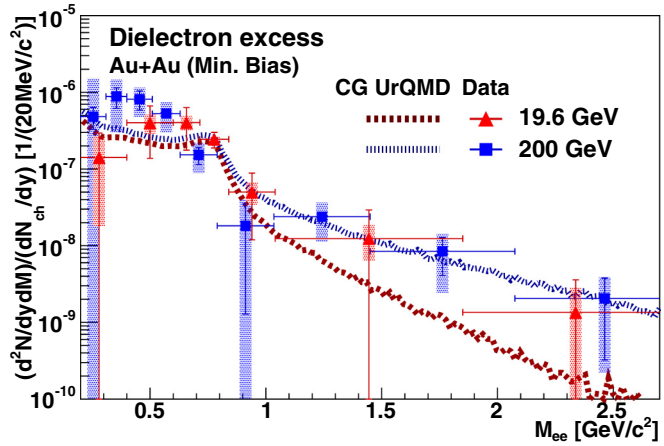

FIG. 5. Dielectron excess spectrum for minimum bias (0%–80% most central) Au + Au collision at $\sqrt{s_{NN}} = 19.6$ and 200 GeV as obtained with the coarse-graining of UrQMD simulations (CG UrQMD). The results include the thermal contributions from the ρ, multipion interactions, and the QGP. Additionally, the UrQMD freeze-out ρ is included for this calculation. The model results are compared to the results of experimental measurements by the STAR Collaboration [15].

is difficult in this region as also a strong contribution from correlated charm decays is found here; see discussion above.

In addition to the full invariant-mass distributions, the STAR Collaboration also published dilepton excess spectra for minimum-bias Au + Au collisions at 19.6 and 200 GeV [15]. Here the cocktail contributions (hadronic decays, Drell-Yan, and open charm) are subtracted such that the resulting spectra represent only the thermal dilepton emission. Furthermore, the data are corrected for the experimental acceptance. In Fig. 5 these results are compared to the thermal contribution from our model, including the nonthermal UrQMD "freeze-out" ρ and excluding the thermal ω contribution. (The ω is usually treated as part of the cocktail and was subtracted from the experimental spectrum.) We see that for the mass region $M_{e^+e^-} > 1$ GeV/c^2 in Au + Au collisions at $\sqrt{s_{NN}} = 200$ GeV the thermal result agrees very well with the data, indicating that the thermal part of this mass region seems to be accurately described with the coarse-graining approach. However, note that the subtracted cocktail contribution does not account for medium modifications of the charm contribution, so that the meaning of the high-mass excess spectrum is rather limited. At 19.6 GeV the thermal spectrum from the model seems to be slightly below the data for higher masses, but still within the large statistical and systematic errors. In the low-mass region the agreement between model and data is better for 19.6 GeV than for 200 GeV, but in both cases the experimental thermal excess seems to be slightly underestimated by the model. Nevertheless, considering the uncertainty of the data and the subtraction procedure, the agreement is quite satisfactory.

So far we have considered dilepton spectra for minimum-bias reactions and the full transverse-momentum range, but the thermal dilepton yield also depends largely on the centrality of the reaction and on the transverse-momentum window in which the results are measured. Both dependencies were investigated by the STAR Collaboration for Au + Au collisions at 200 GeV [14], and the experimental data are presented together with the model results in Fig. 6. The left plot (a) shows the invariant-mass spectra for central (0%–10%), semicentral (10%–40%), and peripheral (40%–80%) collisions, together with the minimum-bias result from Fig. 3(b) for comparison. In all four centrality classes one observes quite a good description of the low-invariant-mass data by the coarse-graining results. For higher masses larger than 1 GeV/c^2 the underestimation of the dilepton yield observed for minimum-bias reactions is also found for other centrality classes. However, for the most central reactions the description seems to be slightly better. In this case the thermal emission alone can almost fully describe the dilepton data for higher masses. This would be in accordance with the assumption that the medium effects on the open charm production are most dominant for central collisions, leading to a suppression of the open-charm contribution to the dilepton spectrum.

For the p_t dependence of e^+e^- production, the comparison between theory and data gives a more nuanced picture, as presented in Fig. 6(b). Here the scaled results for minimum-bias Au + Au collisions in four different transverse momentum bins are shown. In the low-invariant-mass region one finds a good description of the data for the lower transverse momentum bins up to 1 GeV/c, while especially for $p_t >$ 1.5 GeV/c the measured results are underestimated by up to a factor 2. Interestingly, this does not only affect the thermal yield, but also the pure hadronic cocktail contributions, as can be seen from the underestimate for the π-dominated very low masses and the ω and ϕ peaks. The reason for this might be the expansion dynamics from the underlying transport model, which is known to somewhat underestimate the collective flow of the fireball [48], resulting in too soft p_t spectra for the

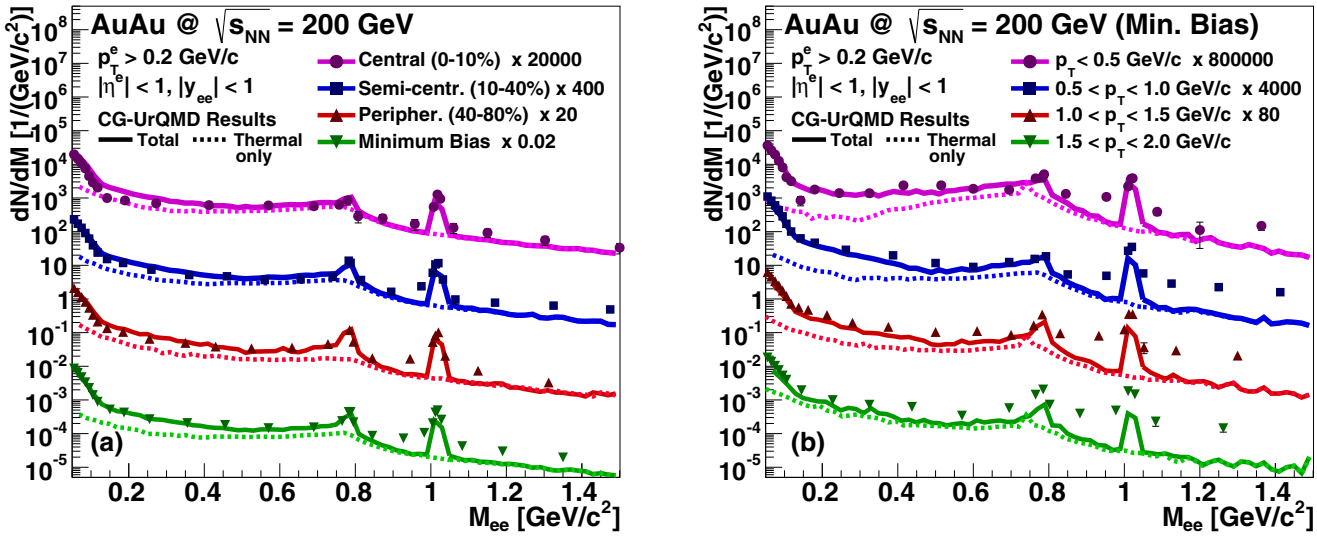

FIG. 6. Dielectron invariant-mass spectra for Au + Au collisions at $\sqrt{s_{NN}} = 200$ GeV for different centralities (a) and transverse-momentum bins (b). Besides the total yields (solid lines), we also show the thermal contribution separately (dashed lines). The results in (a) are shown for central (0%–10%), semicentral (10%–40%), peripheral (40%–80%), and minimum-bias (i.e., 0%–80%) events. In (b) the spectra are shown for minimum bias collisions in four transverse-momentum bins covering the range from $p_t = 0$ to 2.0 GeV/c. The spectra are shown within the STAR acceptance and compared to the experimental data [14]. In addition, they are scaled for better comparability.

produced particles. However, the general trend when going from the low- to the high-transverse-momentum region is the increasing importance of the thermal emission in the low-mass region and a flattening of the shape of the spectrum. This is attributable to two effects: On the one hand, the p_t^e cut for single electrons leads to a suppression of low masses ($M_{e^+e^-} < 0.4$ GeV/c^2) when the transverse momentum of the pair is close to zero. On the other hand, the emission of high-p_t dileptons occurs mostly at the higher temperatures that can be found in the early quark-gluon plasma phase, whereas the hadronic emission is usually found to be softer.

Regarding the higher invariant-mass region for $M_{e^+e^-} > 1$ GeV/c^2, an underestimation of the thermal yield is visible, reaching from a factor 2 for low p_t up to a factor of 10 for the higher transverse momenta. This underprediction is not surprising, as it was already visible in the full p_t-integrated invariant-mass spectrum. As mentioned above, this is clearly attributable to the absence of the charm and Drell-Yan contributions in our calculation.

Although we have up to this point focused on the measurements by the STAR Collaboration, it is natural to compare the model results obtained from the coarse-graining approach also with the results of the PHENIX Collaboration. This is of importance because the first results from PHENIX showed a strong enhancement of the dilepton invariant-mass spectrum for $0.3 < M_{e^+e^-} < 0.7$ GeV/c^2 in central collisions, which was not compatible with the results from the STAR Collaboration [100]. In consequence, there has been much discussion about the different detector properties and corresponding acceptances, which made a direct comparison of the two results difficult. Also, theoretical models failed to reproduce the PHENIX results [27,101]. Recently, the PHENIX Collaboration published new results measured with an updated experimental setup, including a hadron-blind detector (HBD) that could significantly improve the electron identification and the signal sensitivity [16]. In Fig. 7 we show the model results for both central and minimum-bias Au + Au collisions at $\sqrt{s_{NN}} = 200$ GeV within the PHENIX and STAR acceptances, together with the corresponding experimental data. The comparison clearly shows that the model not only describes the STAR data, but also the new PHENIX results for

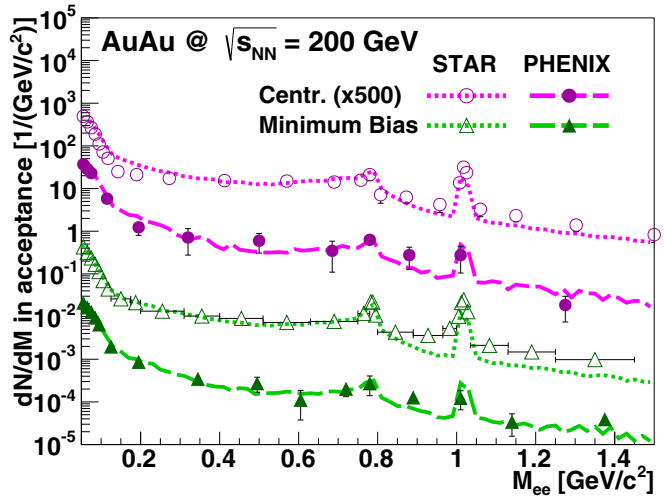

FIG. 7. Comparison of the dielectron invariant-mass spectra for central (magenta lines) and minimum-bias (green lines) Au + Au collisions at $\sqrt{s_{NN}} = 200$ GeV with the STAR and PHENIX data [14,16] in the corresponding acceptances. The total sum of the model results for PHENIX is given by the long dashed lines, and those for STAR are given by the short dashed lines.

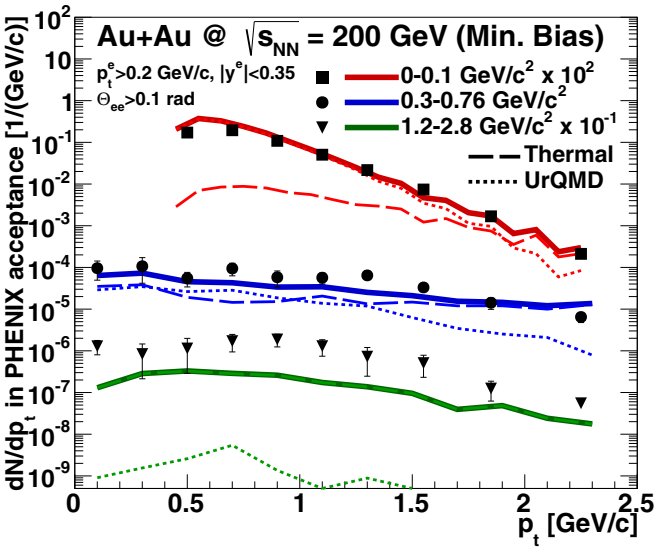

FIG. 8. Dielectron transverse-momentum spectra for three mass bins (red lines, $M = 0$–0.1 GeV/c^2; blue lines, $M = 0.3$–0.76 GeV/c^2; green lines, $M = 1.2$–2.8 GeV/c^2) within the PHENIX acceptance. The results here are for minimum-bias Au + Au collisions at $\sqrt{s_{NN}} = 200$ GeV. Besides the total yields from the model calculations (solid lines) also the thermal parts (long dashed lines) and the nonthermal hadronic decay contributions (short dashed lines) are presented separately. For comparison, the experimental data from the PHENIX Collaboration [16] are shown as well.

central as well as minimum-bias collisions. However, note that the statistics obtained by PHENIX is significantly lower, leading to larger errors of the measurement. The main explanation for this is the two-arm setup of the PHENIX detector where many of the produced electrons and positrons do not reach the detector; if only one particle of a pair reaches the detector, this further increases the background of the measurement. Nevertheless, within the errors of the measurement one can state that the PHENIX and STAR dilepton measurements now fully agree with each other and that the low-mass excess above the hadronic cocktail can be explained by thermal hadronic and partonic emission from medium-modified spectral functions.

To conclude the study for RHIC energies, the model results are finally compared to the transverse-momentum spectra from the PHENIX measurement in Fig. 8. The (scaled) data and model results within experimental acceptance are presented for three different invariant-mass bins. The thermal contribution and the hadronic decay cocktail from UrQMD are shown separately, as well as the total yield. At very low masses ($M_{e^+e^-} < 0.1$ GeV/c^2) the hadronic cocktail contribution dominates the dilepton emission, mainly stemming from π^0 decays. Only for high p_t larger than 1.5 GeV/c does the thermal emission become significant. However, such high momenta are largely suppressed by a factor of 100 in that mass region. The model results agree quite well with the experimental measurements, only for lower p_t a slight overestimation of the yield is obtained. (Note that dilepton pairs with $p_t^{ee} < 0.4$ GeV/c are out of the PHENIX acceptance in this mass bin, as the single-electron transverse momentum is required to be larger than 0.2 GeV/c.) In the mass region from 0.3 to 0.76 GeV/c^2 the thermal and nonthermal emissions almost equally contribute for low p_t with a slight dominance of the hadronic cocktail for transverse momenta from 0.5 to 1.0 GeV/c. In contrast, the thermal dilepton emission clearly outshines the hadronic decays for higher p_t values above 1.5 GeV/c. Note that the present findings from the coarse-graining approach for this mass region roughly agree with the results from a fireball parametrization (using the same spectral functions as in our model) where the nonthermal emission dominates for lower momenta and the thermal contribution—mainly from the ρ—for higher momenta [16]. For the mass region $M_{e^+e^-} > 1.2$ GeV/c^2 the thermal emission (i.e., here almost exclusively the partonic contribution from the QGP) is clearly the dominant source in the present calculations. However, the yield obtained with the coarse-graining approach is below the data by about a factor 2–3 for low p_t and up to 10 for higher momenta, once again indicating the missing contributions from open-charm mesons. In spite of the significantly differing acceptances of the STAR and PHENIX experiments, the outcome presented in Fig. 8 is consistent with the findings from the comparison of model results and data for the invariant-mass spectra in various p_t bins [see Fig. 6(b)].

C. Large Hadron Collider

As became clear from the study of the reaction dynamics in Sec. III A, the fireball of hot and dense matter created in a heavy-ion collision reaches higher temperatures and cools down more slowly at the Large Hadron Collider in comparison to the reaction evolution for RHIC energies. However, there is no significant change with regard to the baryon densities, the baryochemical potential was already close to zero for most cells at $\sqrt{s_{NN}} = 200$ GeV. Consequently, the resulting invariant-mass spectra for central (0%–10%) Pb + Pb collisions at center-of-mass energies of 2.76 and 5.5 TeV as shown in Fig. 9 exhibit the same mostly vacuumlike spectral shape of the ρ meson contribution, together with an increased yield stemming from the quark-gluon plasma. The partonic contribution is dominating the spectra for masses above 0.1 GeV/c^2, except for the pole-mass peaks of the three vector mesons ρ, ω, and ϕ. However, the ρ contribution still plays a significant role as well, and its relative strength is not much smaller than at the top RHIC energy. In general, the increasing number of hot cells with temperature above T_c goes along with a longer lifetime of the fireball and a larger overall thermal four-volume also for temperatures below the critical temperature, which equally leads to a rise of the hadronic emission. In the same manner as there is no strong change of the spectra from RHIC to LHC, the situation does hardly change when going from 2.76 TeV to the maximum LHC energy of 5.5 TeV, except for a higher overall yield. We study this energy dependence in more detail in Sec. III D.

The transverse-momentum spectra for 2.76 TeV in Fig. 10 are shown in two different mass bins, for the low-mass region ($0.2 < M_{e^+e^-} < 0.9$ GeV/c^2) and for the intermediate masses above the ϕ pole mass ($1.05 < M_{e^+e^-} < 2.5$ GeV/c^2). For the lower masses the finding is similar to those for Au + Au collisions at 200 GeV (compare Fig. 8): The non-thermal

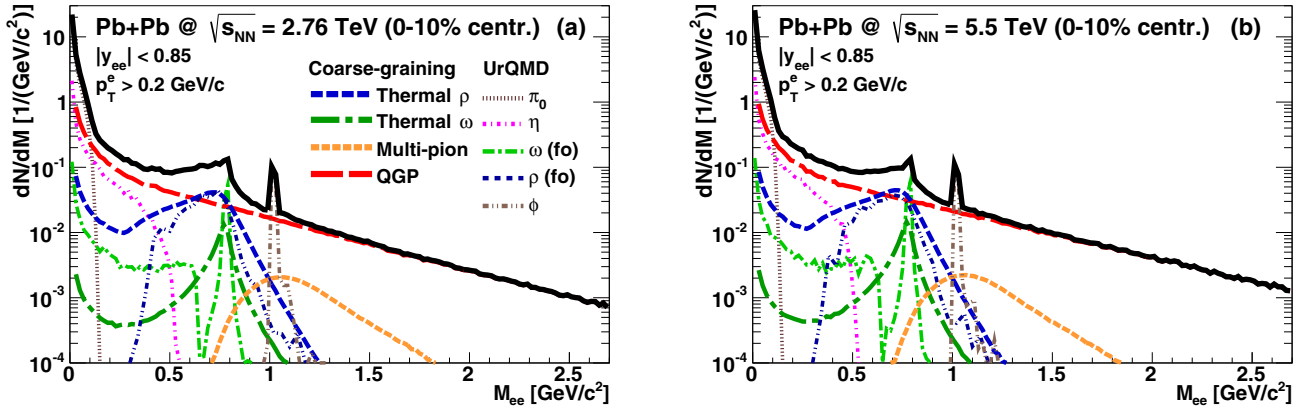

FIG. 9. Dielectron invariant-mass spectra for 0%–10% most central Pb + Pb collisions at $\sqrt{s_{NN}} = 2.76$ TeV (a) and 5.5 TeV (b). The sum includes the thermal hadronic and partonic emission obtained with the coarse-graining approach and also the hadronic π, η, and ϕ decay contributions from UrQMD as well as the "freeze-out" contributions (from cold cells) of the ρ and ω mesons.

hadronic sources stemming from meson decays in UrQMD are more dominant at low p_t, while the thermal emission is the major contribution for high momenta. In general, the slope of the thermal emission is harder (i.e., flatter) than that of the hadronic decays. For the intermediate mass region above 1 GeV/c^2, the only dominant contribution stems from the quark-gluon plasma, whereas the non-thermal part becomes negligible. The overall slope of the higher masses is also harder, indicating emission from hotter cells, but also the stronger flow which is proportional to the mass of the particles. As before, one should, however, bear in mind that a full study for the high masses would need to include the missing charm and Drell-Yan contributions.

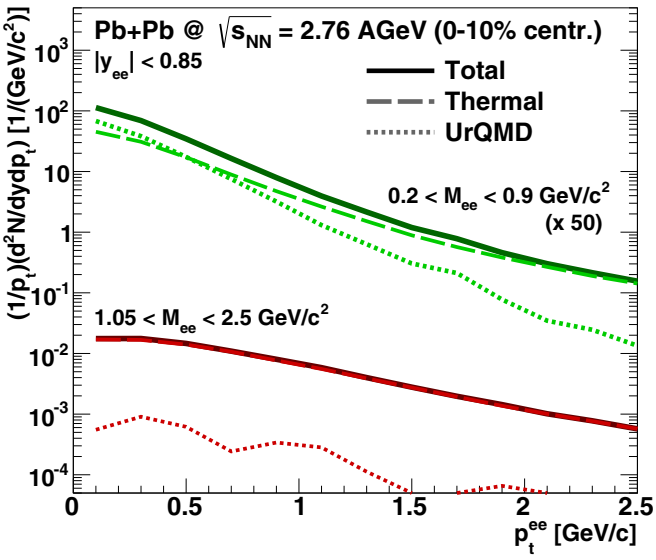

FIG. 10. Dielectron transverse-momentum spectra for central Pb + Pb collisions at $\sqrt{s_{NN}} = 2.76$ TeV. The results are shown for the low-mass ($0.2 < M_{e^+e^-} < 0.9$ GeV/c^2; green lines) and intermediate mass region ($1.05 < M_{e^+e^-} < 2.5$ GeV/c^2; red lines). Besides the total yields from the model calculations (solid lines), also the thermal (long dashed lines) and nonthermal UrQMD hadronic decay contributions (short dashed lines) are presented.

D. Comparison of RHIC and LHC results

The previous results have already shown that the temperature and lifetime of the fireball increase when going from RHIC to LHC energies, which is connected with a larger yield from thermal dilepton production. In the following, these very qualitative findings shall be investigated in more detail.

In Fig. 11(a) the relative ratio of the thermal dilepton yield for central collisions at midrapidity ($|y_{ee}| < 1$) in different mass regions is shown in relation to the yield which is obtained for Au + Au at $\sqrt{s_{NN}} = 200$ GeV. In addition, the increase of the π^0 yield is shown to provide a comparison of the rise in the thermal yield with the one of the freeze-out hadron yield (or dilepton yield from hadronic decays, respectively). The results depict that, in general, the thermal contributions exhibit a stronger increase than the π^0 yield. For the lower masses—0.05 to 0.3 and 0.3 to 0.6 GeV/c^2—the thermal yield scales with the number of neutral pions as $N_{\pi^0}^{\alpha}$, with α found to be approximately 1.9 here. For the mass region above the ϕ pole mass, where almost purely the QGP contributes to the thermal emission, the relative increase is even stronger with $\alpha \approx 2.4$. Note that the exponent α for the mass region where the excess above the cocktail is found (i.e., 0.3–0.6 GeV/c^2) is similar and only slightly larger compared to the one obtained using a fireball parametrization [11]; there the scaling with the total number of charged hadronic particles is found to be $N_{\rm ch}^{\alpha}$ and $\alpha = 1.8$. The somewhat stronger enhancement of the high-mass yield at LHC energies is explained by the fact that the number of QGP-emitting hot cells exhibits a larger increase than the lower temperature four-volume (compare Figs. 1 and 2).

Whereas the thermal yields alone allow for only rather qualitative conclusions regarding the underlying reaction dynamics, another observable that helps to determine the temperature and expansion dynamics of the created fireball is the slope of the transverse-mass spectra ($m_t = \sqrt{M_{ee}^2 + p_t^2}$). The effective slope parameter $T_{\rm eff}$ can be extracted using the

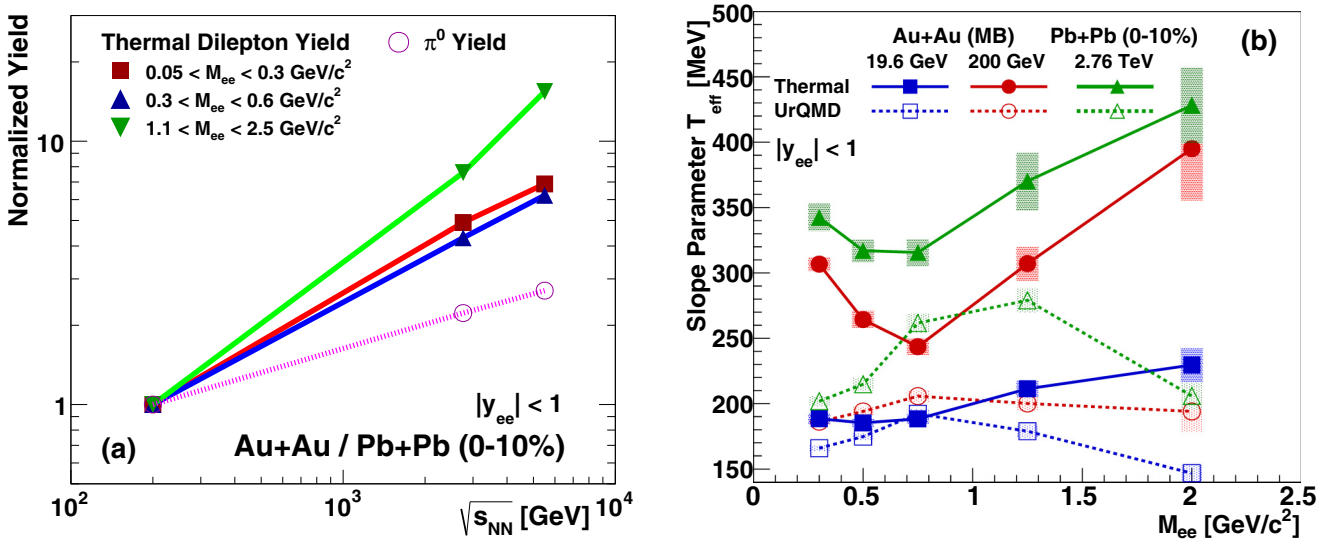

FIG. 11. (a) Thermal dilepton yield for three different mass regions and the π^0 yield for central Au + Au/Pb + Pb collisions, normalized to the result for $\sqrt{s_{NN}} = 200$ GeV. (b) Mass-dependent slope parameter $T_{\rm eff}$ for the thermal (solid lines) and nonthermal (dashed lines) dilepton yields in minimum-bias Au + Au collisions at 19.6 GeV (blue lines) and 200 GeV as well as for central Pb + Pb at 2.76 TeV (green lines). The error bands indicate the systematic error of the fit. All results are for midrapidity, i.e., for $|y_{ee}| < 1$.

fit function [102]

$$\frac{dN}{m_t dm_t} = C \exp\left(-\frac{m_t}{T_{\rm eff}}\right). \tag{12}$$

Note that $T_{\rm eff}$ must not be confounded with the temperature of the medium, as the transverse-momentum distribution from a thermal source is not only determined by the temperature: The radial flow of the system leads to a significant blueshift of the m_t spectra as well [11]. The effective slope parameter for the thermal and hadronic cocktail (UrQMD) contributions at midrapidity for Au + Au and Pb + Pb collisions at three different energies ($\sqrt{s_{NN}} = 19.6$, 200, and 2760 GeV) is shown in Fig. 11(b). The results are presented for different mass bins ranging from 0.2 to 2.5 GeV/c^2. To obtain $T_{\rm eff}$ the spectra were fitted in mass-dependent m_t ranges corresponding to $0.5 < p_t < 1.8$ GeV/c. Interestingly, the results exhibit completely different mass dependencies for thermal and nonthermal contributions. $T_{\rm eff}$ of the nonthermal decay contributions reaches a maximum around the ρ and ω pole masses (for RHIC energies) or around 1–1.5 GeV/c^2 (at LHC) and falls off when going to lower or higher energies. Conversely, the slope parameter of the thermal contributions drops with increasing mass or remains at the same level up to approximately 1 GeV/c^2 and then it shows a strong rise for higher masses.

The different mass dependency of $T_{\rm eff}$ for the thermal and nonthermal decay contributions can be explained by the different conditions of emission: Where the thermal source is mainly of hadronic nature, i.e., especially around the ρ and ω pole masses, one finds a lower average emission temperature, compared to the mass ranges dominated by the partonic contribution. This effect is reflected in the thermal m_t slopes. The increase of $T_{\rm eff}$ for masses above 1 GeV/c^2 is attributable to the fact that the thermal high-mass emission is suppressed at lower temperatures. In contrast, the nonthermal hadronic decays mostly occur at a late stage of the fireball evolution, outside the hot and dense region. This leads to, in general, lower slope parameters obtained for the nonthermal contributions compared to the thermal ones. However, note that there is a difference between the contributions from the long-lived low-mass π^0 and η mesons, for which one finds the lowest $T_{\rm eff}$, and especially the very short-lived freeze-out ρ contribution. In spite of the fact that here the ρ stems only from cells where no thermal emission is assumed, in its pole-mass region one finds a harder slope than at the π^0- and η-dominated low masses. A reason might also be that these ρ mesons carry additional momentum owing to their rather late and peripheral origin, compared to the other mesons. The decrease for higher masses above 1 GeV/c^2—which are dominated by the ϕ and still some ρ—might be explained by the kinematics of the microscopic decay processes, where high momenta are naturally suppressed if a particle with higher mass is produced, and the longer lifetime of the ϕ compared to the ρ meson.

The slope parameters for the thermal emission from the coarse-graining approach are similar to those from a fireball parametrization [11] for RHIC energies, but for the LHC they seem to be somewhat smaller. However, as already mentioned, it is known that the flow effects are underestimated within the UrQMD model at high collision energies [48], so that these differences should be mainly owing to a less distinct expansion of the system and not to differences in the average temperature. The same conclusion is suggested by the comparison of dilepton spectra with experimental data, where we saw an underestimation of the yield for high p_t [see, e.g., Fig. 6(b)].

IV. CONCLUSIONS AND OUTLOOK

In this paper we have presented dilepton spectra for energies available at RHIC and LHC, obtained with an approach using coarse-grained UrQMD transport simulations to calculate the

thermal dilepton emission. The results for RHIC energies are compared with the experimental data from the STAR and PHENIX Collaborations and show good agreement. Furthermore, we could depict that the newest PHENIX results collected with the HBD upgrade of the detector are now fully consistent with the STAR measurements and that both can be reproduced within the coarse-graining approach. The excess above the hadronic cocktail in the region for $0.3 < M_{e^+e^-} < 0.7$ GeV$/c^2$ is hereby explained by thermal emission from a broadened ρ and the quark-gluon plasma.

For higher masses above the ϕ peak our results lie by tendency somewhat below the experimental data. This can be mainly ascribed to the missing implementation of the charm emission, which will be the dominant source for these high masses. However, our results show that also the partonic emission gives a significant contribution to the overall yield in this mass region. Furthermore, a comparison of different EoSs indicates that the thermal dilepton spectrum for $M_{e^+e^-} > 1$ GeV$/c^2$ might enable one to draw conclusions with regard to the QCD phase structure and the equation of state if the charm contribution can be reliably subtracted. The present results are consistent with the open-charm dilepton spectra obtained using a Langevin approach to simulate the in-medium effects on the invariant-mass spectra in a transport + hydro hybrid model. These simulations indicate a strong suppression of the open-charm contribution in hot and dense matter compared to the vacuum case, finally making up only roughly 50% of the total high-mass yield at RHIC [39]. In consequence, a study of dilepton emission including the charm contribution in the coarse-graining approach would be very instructive for the full understanding of dilepton emission patterns for higher masses and is planned for future investigations.

While the energy and centrality dependence of the low-mass dilepton production is well reproduced within the model, the transverse-momentum dependence shows some deviations from the measurement for higher p_t, whereas the (dominant) low-momentum production is quite well described. This effect is probably connected to an underestimation of the collective flow in the underlying transport model. One should bear in mind that the model is purely hadronic and that it might therefore not be able to describe some of the dynamical effects adequately which are attributable to the emergence of a partonic phase. However, considering the hadronic nature of the model, the agreement with experimental data as well as the spectra from fireball parametrizations is surprisingly good. In consequence, this substantiates the basic idea of the coarse-graining approach, namely that the only necessary information regarding the fireball evolution is the distribution of energy and particle densities (or T and μ, respectively) if one wants to determine the dilepton emission.

Together with the previous results for energies available at SIS 18, FAIR, and CERN-SPS, the coarse-graining approach has proven to be a successful tool for the theoretical description of dilepton production in heavy-ion collisions over the whole domain of presently available energies, corresponding to a range of $\sqrt{s_{NN}}$, which spans over three orders of magnitude. It is, nevertheless, also apparent that the coarse-graining approach in its present form cannot fully substitute a study of the QCD phase structure based on a microscopic picture of the fireball evolution including the effects from the creation of a deconfined phase of quasifree quarks and gluons. This will be important, e.g., for the study of the anisotropic flow of electromagnetic probes.

ACKNOWLEDGMENTS

The authors especially thank Ralf Rapp for providing the parametrizations of the spectral functions. S.E. acknowledges Jan Steinheimer for valuable and fruitful discussions. This work was supported by the Hessian Initiative for Excellence (LOEWE) through the Helmholtz International Center for FAIR (HIC for FAIR), the Bundesministerium für Bildung und Forschung, Germany (BMBF), and the Helmholtz-Gemeinschaft through the Research School for Quark-Matter Studies (H-QM). The computational resources for this work were provided by the LOEWE-CSC.

[1] H. Stöcker and W. Greiner, Phys. Rep. **137**, 277 (1986).
[2] P. Danielewicz, R. Lacey, and W. G. Lynch, Science **298**, 1592 (2002).
[3] E. Shuryak, Prog. Part. Nucl. Phys. **62**, 48 (2009).
[4] R. Rapp, J. Wambach, and H. van Hees, in *Relativistic Heavy Ion Physics*, edited by R. Stock, Landolt-Börnstein-Group I Elementary Particles, Nuclei and Atoms Vol. 23 (Springer, Berlin, 2010), pp. 134–175.
[5] J. Schukraft and R. Stock, in *60 Years of CERN Experiments and Discoveries*, edited by H. Schopper and L. Di Lella (World Scientific, Singapore, 2015), Chap. 3, pp. 61–87.
[6] J. D. Bjorken, Phys. Rev. D **27**, 140 (1983).
[7] E. L. Feinberg, Nuovo Cimento A **34**, 391 (1976).
[8] E. V. Shuryak, Phys. Lett. B **78**, 150 (1978).
[9] G. Vujanovic, C. Young, B. Schenke, R. Rapp, S. Jeon, and C. Gale, Phys. Rev. C **89**, 034904 (2014).
[10] R. Ryblewski and M. Strickland, Phys. Rev. D **92**, 025026 (2015).
[11] R. Rapp, Adv. High Energy Phys. **2013**, 148253 (2013).
[12] R. Rapp and H. van Hees, Phys. Lett. B **753**, 586 (2016).
[13] L. Adamczyk *et al.* (STAR Collaboration), Phys. Rev. Lett. **113**, 022301 (2014) [Addendum: **113**, 049903 (2014)].
[14] L. Adamczyk *et al.* (STAR Collaboration), Phys. Rev. C **92**, 024912 (2015).
[15] L. Adamczyk *et al.* (STAR Collaboration), Phys. Lett. B **750**, 64 (2015).
[16] A. Adare *et al.* (PHENIX Collaboration), Phys. Rev. C **93**, 014904 (2016).
[17] K. Schmidt, E. Santini, S. Vogel, C. Sturm, M. Bleicher, and H. Stöcker, Phys. Rev. C **79**, 064908 (2009).
[18] J. Weil, H. van Hees, and U. Mosel, Eur. Phys. J. A **48**, 111 (2012).

[19] J. Weil, S. Endres, H. van Hees, M. Bleicher, and U. Mosel, J. Phys. Conf. Ser. **612**, 012039 (2015).
[20] S. Endres and M. Bleicher, J. Phys. Conf. Ser. **426**, 012033 (2013).
[21] E. L. Bratkovskaya, J. Aichelin, M. Thomere, S. Vogel, and M. Bleicher, Phys. Rev. C **87**, 064907 (2013).
[22] B. Schenke and C. Greiner, Phys. Rev. C **73**, 034909 (2006).
[23] B. Schenke and C. Greiner, Phys. Rev. Lett. **98**, 022301 (2007).
[24] J. Weil, U. Mosel, and V. Metag, Phys. Lett. B **723**, 120 (2013).
[25] E. L. Bratkovskaya, W. Cassing, R. Rapp, and J. Wambach, Nucl. Phys. A **634**, 168 (1998).
[26] E. Bratkovskaya and W. Cassing, Nucl. Phys. A **807**, 214 (2008).
[27] O. Linnyk, W. Cassing, J. Manninen, E. L. Bratkovskaya, and C. M. Ko, Phys. Rev. C **85**, 024910 (2012).
[28] O. Linnyk, E. L. Bratkovskaya, and W. Cassing, Prog. Part. Nucl. Phys. **87**, 50 (2016).
[29] P. Huovinen, M. Belkacem, P. J. Ellis, and J. I. Kapusta, Phys. Rev. C **66**, 014903 (2002).
[30] S. Endres, H. van Hees, J. Weil, and M. Bleicher, Phys. Rev. C **91**, 054911 (2015).
[31] S. Endres, H. van Hees, J. Weil, and M. Bleicher, Phys. Rev. C **92**, 014911 (2015).
[32] S. Endres, H. van Hees, and M. Bleicher, Phys. Rev. C **93**, 054901 (2016).
[33] J. Steinheimer, M. Lorenz, F. Becattini, R. Stock, and M. Bleicher, Phys. Rev. C **93**, 064908 (2016).
[34] S. A. Bass, M. Belkacem, M. Bleicher, M. Brandstetter, L. Bravina *et al.*, Prog. Part. Nucl. Phys. **41**, 255 (1998).
[35] M. Bleicher, E. Zabrodin, C. Spieles, S. A. Bass, C. Ernst *et al.*, J. Phys. G **25**, 1859 (1999).
[36] A. Adare *et al.* (PHENIX Collaboration), Phys. Lett. B **670**, 313 (2009).
[37] H. van Hees and R. Rapp, Phys. Rev. C **71**, 034907 (2005).
[38] T. Lang, H. van Hees, G. Inghirami, J. Steinheimer, and M. Bleicher, Phys. Rev. C **93**, 014901 (2016).
[39] T. Lang, H. van Hees, J. Steinheimer, and M. Bleicher, arXiv:1305.7377[hep-ph].
[40] G. David, R. Rapp, and Z. Xu, Phys. Rept. **462**, 176 (2008).
[41] A. Adare *et al.* (PHENIX Collaboration), Phys. Rev. Lett. **109**, 122302 (2012).
[42] A. Adare *et al.* (PHENIX Collaboration), arXiv:1509.07758[nucl-ex].
[43] H. Petersen, M. Bleicher, S. A. Bass, and H. Stöcker (2008), arXiv:0805.0567[hep-ph].
[44] http://www.urqmd.org
[45] W. M. Yao *et al.* (Particle Data Group), J. Phys. G **33**, 1 (2006).
[46] E. L. Bratkovskaya, M. Bleicher, M. Reiter, S. Soff, H. Stöcker, M. van Leeuwen, S. A. Bass, and W. Cassing, Phys. Rev. C **69**, 054907 (2004).
[47] M. Mitrovski, T. Schuster, G. Graf, H. Petersen, and M. Bleicher, Phys. Rev. C **79**, 044901 (2009).
[48] H. Petersen, Q. Li, X. Zhu, and M. Bleicher, Phys. Rev. C **74**, 064908 (2006).
[49] M. Bleicher and H. Stöcker, Phys. Lett. B **526**, 309 (2002).
[50] X. Zhu, M. Bleicher, and H. Stöcker, Phys. Rev. C **72**, 064911 (2005).
[51] X.-l. Zhu, M. Bleicher, and H. Stöcker, J. Phys. G **32**, 2181 (2006).
[52] Y. Lu, M. Bleicher, F. Liu, Z. Liu, H. Petersen, P. Sorensen, H. Stöcker, N. Xu, and X. Zhu, J. Phys. G **32**, 1121 (2006).
[53] P. F. Kolb, P. Huovinen, U. W. Heinz, and H. Heiselberg, Phys. Lett. B **500**, 232 (2001).
[54] V. P. Konchakovski, E. L. Bratkovskaya, W. Cassing, V. D. Toneev, S. A. Voloshin, and V. Voronyuk, Phys. Rev. C **85**, 044922 (2012).
[55] J. Uphoff, F. Senzel, O. Fochler, C. Wesp, Z. Xu, and C. Greiner, Phys. Rev. Lett. **114**, 112301 (2015).
[56] C. Eckart, Phys. Rev. **58**, 919 (1940).
[57] D. Zschiesche, S. Schramm, J. Schaffner-Bielich, H. Stöcker, and W. Greiner, Phys. Lett. B **547**, 7 (2002).
[58] M. He, R. J. Fries, and R. Rapp, Phys. Rev. C **85**, 044911 (2012).
[59] H. Petersen, J. Steinheimer, G. Burau, M. Bleicher, and H. Stöcker, Phys. Rev. C **78**, 044901 (2008).
[60] J. Steinheimer, V. Dexheimer, H. Petersen, M. Bleicher, S. Schramm, and H. Stöcker, Phys. Rev. C **81**, 044913 (2010).
[61] L. Bravina, E. Zabrodin, M. I. Gorenstein, S. Bass, M. Belkacem *et al.*, Nucl. Phys. A **661**, 600 (1999).
[62] L. Bravina, E. Zabrodin, M. I. Gorenstein, S. Bass, M. Belkacem *et al.*, Phys. Rev. C **60**, 024904 (1999).
[63] W. Florkowski and R. Ryblewski, Phys. Rev. C **83**, 034907 (2011).
[64] W. Florkowski, M. Martinez, R. Ryblewski, and M. Strickland, Nucl. Phys. A **904-905**, 803c (2013).
[65] D. Bandyopadhyay, M. Gorenstein, H. Stöcker, W. Greiner, and H. Sorge, Z. Phys. C **58**, 461 (1993).
[66] P. Koch, Phys. Lett. B **288**, 187 (1992).
[67] R. Rapp and J. Wambach, Adv. Nucl. Phys. **25**, 1 (2002).
[68] U. Heinz, in *Relativistic Heavy Ion Physics*, edited by R. Stock, Landolt-Börnstein-Group I Elementary Particles, Nuclei and Atoms Vol. 23 (Springer, Berlin, 2010), pp. 240–292.
[69] A. Muronga, Phys. Rev. C **69**, 034903 (2004).
[70] A. Muronga, Phys. Rev. C **69**, 044901 (2004).
[71] N. Demir and S. A. Bass, Eur. Phys. J. C **62**, 63 (2009).
[72] N. Demir and S. A. Bass, Phys. Rev. Lett. **102**, 172302 (2009).
[73] T. E. Nemakhavhani and A. Muronga, arXiv:1603.06347[nucl-th].
[74] U. W. Heinz and P. F. Kolb, Nucl. Phys. A **702**, 269 (2002).
[75] M. Gyulassy and L. McLerran, Nucl. Phys. A **750**, 30 (2005).
[76] D. Teaney, Phys. Rev. C **68**, 034913 (2003).
[77] K. Dusling, Nucl. Phys. A **839**, 70 (2010).
[78] M. Dion, J.-F. Paquet, B. Schenke, C. Young, S. Jeon, and C. Gale, Phys. Rev. C **84**, 064901 (2011).
[79] B. Schenke and M. Strickland, Phys. Rev. D **76**, 025023 (2007).
[80] S.-X. Liu, F.-M. Liu, K. Werner, and M. Yue, arXiv:1508.05160[hep-ph].
[81] F.-M. Liu, S.-X. Liu, and K. Werner, arXiv:1512.08833[nucl-th].
[82] C. Shen, U. W. Heinz, J.-F. Paquet, I. Kozlov, and C. Gale, Phys. Rev. C **91**, 024908 (2015).
[83] C. Shen, J.-F. Paquet, U. Heinz, and C. Gale, Phys. Rev. C **91**, 014908 (2015).
[84] J. Cleymans, J. Fingberg, and K. Redlich, Phys. Rev. D **35**, 2153 (1987).
[85] E. Braaten, R. D. Pisarski, and T.-C. Yuan, Phys. Rev. Lett. **64**, 2242 (1990).
[86] H.-T. Ding, A. Francis, O. Kaczmarek, F. Karsch, E. Laermann, and W. Soeldner, Phys. Rev. D **83**, 034504 (2011).

[87] V. L. Eletsky, M. Belkacem, P. J. Ellis, and J. I. Kapusta, Phys. Rev. C **64**, 035202 (2001).
[88] F. Klingl, N. Kaiser, and W. Weise, Nucl. Phys. A **624**, 527 (1997).
[89] L. D. McLerran and T. Toimela, Phys. Rev. D **31**, 545 (1985).
[90] R. Rapp and J. Wambach, Eur. Phys. J. A **6**, 415 (1999).
[91] R. Rapp (private communication).
[92] H. van Hees and R. Rapp, Nucl. Phys. A **806**, 339 (2008).
[93] R. Baier, M. Dirks, and K. Redlich, Acta Phys. Pol. B **28**, 2873 (1997).
[94] R. Baier, M. Dirks, K. Redlich, and D. Schiff, Phys. Rev. D **56**, 2548 (1997).
[95] M. Dey, V. Eletsky, and B. L. Ioffe, Phys. Lett. B **252**, 620 (1990).
[96] H. van Hees and R. Rapp, Phys. Rev. Lett. **97**, 102301 (2006).
[97] N. M. Kroll and W. Wada, Phys. Rev. **98**, 1355 (1955).
[98] L. G. Landsberg, Phys. Rep. **128**, 301 (1985).
[99] G.-Q. Li and C. M. Ko, Nucl. Phys. A **582**, 731 (1995).
[100] A. Adare *et al.* (PHENIX Collaboration), Phys. Rev. C **81**, 034911 (2010).
[101] R. Rapp, AIP Conf. Proc. **1322**, 55 (2010).
[102] T. Renk and J. Ruppert, Phys. Rev. C **77**, 024907 (2008).